IL NUOVO CIMENTO Vol. ?, N. ? ?

Cold Ions in Space

Ferdinand Schmidt-Kaler([1]), Peter Wolf([2]), Patrick Gill([3])

([1]) *Institut für Quanten Informationsverarbeitung, Universität Ulm, Albert-Einstein-Allee 11, D-89069 Ulm, Germany*
([2]) *LNE-SYRTE, Observatoire de Paris, CNRS, UPMC, 61 av. de l'Observatoire, 75014 Paris, France*
([3]) *National Physical Laboratory, Hampton Road, Teddington TW11 0LW, United Kingdom*

Summary. — Accurate optical frequency standards employ single trapped and laser cooled ions, we review recent experiments. Optical frequencies can be measured with fractional uncertainties of only a few parts in 10^{17} demonstrating the most accurate clocks available today. Demonstrated quantum information techniques help to further improve on determining residual systematic errors. Additionally, entanglement is also demonstrated to increase the signal to noise ratio. For generating the entanglement of a large number of ions, novel ions traps are currently developed which will allow for a coherent manipulation of the order of 10 to 50 ions.
As one application of this mature technology, we outline a space mission investigating all aspects of gravity in the outer solar system, using an single ion clock as one of the main onboard instruments. We describe the mission and its major scientific goals centered on tests of fundamental physics and exploration of outer solar system objects. It will allow tests of special and general relativity with unprecedented sensitivity and will yield detailed information on the Kuiper belt circumsolar disk.

04.80.-y, 03.30.+p, 06.30.Ft, 96.30.Xa, 32.80.Pj

1. – Introduction

Providing the basic units of time and length in the *systeme internationale* remains one of the important requirements of physics. Over the last several decades, impressive advances in this area have taken advantage from atomic physics and quantum optics. Especially the atomic and quantum optical sections can look back to an impressive history of progress. Most important is the technique of separated oscillatory fields, as introduced by Norman Ramsey([1]) to improve the resolution of spectroscopy in his atomic beam machines. The invention of dynamical trapping allowed Wolfgang Paul([2]) to confine ions for long times and laid the basis of modern ion clocks. Optical cooling techniques and technical developments for laser sources allowed to observe a single ion and to cool its motion to the ground state of the trap potential given solely by the Heisenberg uncertainty principle. A major road block was removed by Theodor Hänsch([3]) and John Hall([4]) with their invention of the femto-second frequency-comb technique to measure accurately optical frequencies. We have seen amazing improvements for optical frequency standards, which may be complemented in future by space-missions where special and general relativity could be tested with many orders of magnitude improvement compared to previous experiments.

The Ramsey technique employs two pulses of electromagnetic excitation to find out about the energy difference of two states of an atom. The first pulse excites a superposition of ground and excited state $|g\rangle + e^{i\psi_0}|e\rangle$ which then evolves in phase during the interaction free period according to the energy difference $\hbar\omega_{eg} = \Delta E = E_e - E_g$. Then, with a time delay of t_{Ramsey} the second pulse of excitation may further rotate the atomic state depending on the phase relation $\Delta\omega$ between electric field $\vec{E}e^{i\omega t}$ and atomic superposition state. Finally, the atom is projected onto the eigenstate basis $\{|g\rangle, |e\rangle\}$. The measured probability p_e allows locking the electromagnetic field frequency ω precisely to the resonance frequency $\omega_{eg} = \Delta E/\hbar$ of the atomic clock transition. The Allan variance $\sigma(\tau)$ indicates the relative frequency deviation of an atomic clock for all timescales, and helps to characterize its performance.

$$\sigma(\tau) = \frac{1}{\pi Q}\sqrt{\frac{T_c}{\tau}}\sqrt{\frac{1}{N} + \gamma} \tag{1}$$

A good performance is reached with an atomic transition with high $Q = \omega_0/\delta\omega$, indicating a clear advantage of optical clock transitions with high transition frequency ω_0 and narrow linewidth $\delta\omega$. The signal improves with the number of atoms like $\sqrt{N}$, provided that the bandwidth γ of the interrogation electromagnetic field is narrow. σ improves with the square-root of the ratio of averaging time τ and clock cycle time T_c. Shot noise limited operation of the Cs-microwave clock has been observed [1]. For very long integration times, however, $\sigma(\tau)$ levels out at a constant minimum σ_{min}, and may even increase again for longer τ due to long term instabilities causing a drift of control parameters (not shown in equ. 1 but discussed later).

Clocks based on single trapped and laser cooled ions show the best performance today,

---

([1]) Nobel Prize in Physics 1989
([2]) Nobel Prize in Physics 1989
([3]) Nobel Prize in Physics 2005
([4]) Nobel Prize in Physics 2005

as the systematic error sources are well under control. Long interrogation times t_{Ramsey} are realized yielding a high resolution with small values of $\delta\omega$; the wavelenghts of the clock transitions are in the optical, even UV region, such that high Q values of the order of 10^{14} are reached. However, with only a single ion, $N = 1$, relatively long integration times τ are necessary. The alternative, a sample of $N \simeq 10^5 - 10^6$ free neutral atoms reaches lower values of $\sigma(\tau)$ more quickly, however on the expense of larger systematic uncertainties and a shorter t_{Ramsey}. A compromise of both approaches are lattice clocks where the neutral atoms are trapped by optical fields without disturbing the optical clock transition [2, 3, 4, 5]. Typical atom clocks employ transitions between long lived energy levels. Using $m_g = 0 \rightarrow m_e = 0$ clock transitions reduces the susceptibility to ambient magnetic field fluctuations.

The paper is organized as follows: In Sect. **2** we illustrate the progress of ion based clocks on the examples of the single ion Hg^+ and the single ion Sr^+ clocks. One of their major systematic error source, the electric quadrupole shift is outlined. Sect. **3** introduces demonstrated quantum information technologies which enable classical frequency measurement techniques to be surpassed. In Sect. **3**˙2, we report how the electric quadrupole shift is measured using an entangled pair of Ca^+ ions. Entangled states of three Be^+ ions lead to Heisenberg limited spectroscopy (Sect. **3**˙3) and quantum logic operations allow using the clock transition of an Al^+ ion read out by a Be^+ ion. Quantum information with ions requires novel segmented ion traps which are briefly sketched in Sect. **4**. The paper is concluded in Sect. **5** with the outline proposal for a space mission "SAGAS" where we focus on the ion clock segment.

2. – The progress of ion clocks

The "electron shelving" technique employs a dipole allowed transition $S_{1/2} \rightarrow P_{1/2}$ or $P_{3/2}$. The ion emits photons at a rate of order 100 MHz when excited by resonant laser radiation. If this laser is tuned to the red side of the resonance, ions are Doppler-cooled to mK temperatures. In the harmonic (pseudo)-potential of the trap with trap frequencies of few MHz this temperature corresponds to a mean vibration quantum number of the order of 10 phonons.

The measurement cycle [6, 7, 8] for an ion clock (Fig. 1) consists of five steps: (i) Excitation of the narrow clock transition, e. g. a $S_{1/2} \rightarrow D_{5/2}$ quadrupole transition in Hg^+, Sr^+, Ca^+, Yb^+ or the intercombination line in In^+. All other light fields are switched off during this step. The excitation might be performed by two time-separated pulses for Ramsey spectroscopy. (ii) The Dipole-allowed transition is excited with the cooling and state detection laser, and a photomultiplier or CCD camera records the

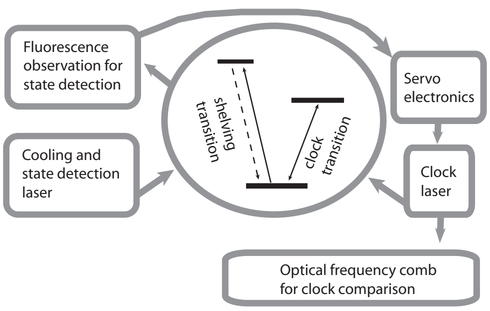

Fig. 1. – Scheme of an ion clock: Basic components are the trapped ion with clock and electron shelving transition, state detection laser, and clock laser which is regulated from the integrated Ramsey signal. Optionally, an optical frequency comb allows for a transfer of the clock frequency.

emitted fluorescence. If the ion emits photons, the ground state of the clock transition, e.g. the $S_{1/2}$ state, is revealed. If the ion does not emit fluorescence, we conclude that the excitation to the upper clock state was successful. Note that this state discrimination quality is close to unity, exceeding 99% typically.(iii) The ion is pumped back to the electronic ground state of the clock transition, and (iv) laser cooling of the vibrational degrees is applied. (v) Optical pumping is applied such that the lower clock state is occupied. Averaged over many repetitions, a Ramsey signal is generated which serves to stabilize the frequency of the laser source driving the clock transition. An optical frequency comb allows the comparison of the optical clock transition frequency with any secondary frequency standard.

In a series of impressive steps during the last decade [16], the ^{199}Hg^{+} clock reached today a systematic frequency uncertainty below 7.2 10^{-17} [12] and has surpassed the performance of the microwave Cesium clock. The Allan deviation reaches $\sigma(\tau) = 10^{-15}$ of relative uncertainty to an independent neutral atom Calcium Ramsey interferometer already at an averaging time of $\tau \simeq$1 minute [17], which surpasses the best Cesium microwave clock. For a further improvement it is necessary to reduce systematic error sources. Indeed, 70% of the uncertainty of the ^{199}Hg^{+} clock stems from the electric quadrupole (EQ) shift of the clock transition [12]. The uncertainty of the nulled EQ-shift for the quadrupole clock transition in the single $^{88}Sr^{+}$ ion clock is estimated to be smaller than this [13], although there are more dominant perturbations such as the black-body shift in this case. The EQ-shift depends on the interaction of the upper clock state $D_{5/2}$ electronic charge distribution with the quadrupole electric field serving to confine the ions in the Paul trap. With different orientations of the $D_{5/2}$ state as denoted by its quantum number $|m\rangle$ the interaction with the trap electric field varies. Therefore the angle β between the magnetic field and quadrupole field axis, the Zeeman sublevel in the $D_{5/2}$ state, and a matrix element $\langle D_{5/2}|r^2|D_{5/2}\rangle$ for the chosen element determine the amplitude of the EQ-shift. Under certain conditions, this shift can be 1..10 Hz [9, 10]. The EQ-shift only reduces to zero if it is averaged over any three mutually precisely perpendicular orientations of the magnetic field, or using a fixed magnetic field, over three sets of Zeeman components in the $D_{5/2}$ state [11, 14]. In the first case, the cancellation relies on the exact knowledge of the orthogonality of magnetic field directions at the location of the ion, and in the second case (applicable to even isotope ions), on the stability of the fixed field during the period of measurements. In this second case, one should expect to cancel the EQ-shift at the sub-% level, provided field stabilities of $\sim$nT can be maintained at the ion.

An alternative method of EQ-shift determination can be achieved using two entangled ions simultaneously exposed to the same electric field of the Paul trap and to the very same magnetic field such that the EQ-frequency shift from different magnetic sublevels is sensed in parallel with both ions. In sect. **3**˙2 we will discuss how two-ion entangled states offer a determination of the quadrupole shift with a relative error of 0.5%.

3. – Quantum computing techniques are improving ion clocks

One of the important branches of interest in quantum information processing is focused to the improvement of an atomic frequency measurement. As the relevant quantum techniques for entangling operations and logic gates [26, 27] in multi-ion crystal have been established, such that a high fidelity is reached, the corresponding applications are emerging. We will discuss briefly the generation of two-ion entangled states and their use for measuring the quadrupole shift in Ca^{+}. In this way, quantum technology helps improving to cure systematic errors of an ion clock. Then, in sect. **3**˙3 we will describe how entangled states help to increase the signal to noise ratio of an ion clock, and how quantum techniques allow investigating new atomic species for the purpose of an ion clock.

The narrow optical clock transition, or a Raman transition between ground state levels allows to coherently manipulate the ions internal electronic state and the common vibrational quantum state. By manipulating the **common vibrational state** as a quantum bus, internal electronic states become entangled.

3˙1. *Long lived Bell states.* – Entanglement of quantum systems means that individual properties of subsystems are unknown but quantum correlations of both subsystems are fully determined. For a crystal of two ions, four Bell states

$$\Psi_\pm = \frac{1}{\sqrt{2}}(|S_{1/2}\rangle_1|D_{5/2}\rangle_2 \pm |D_{5/2}\rangle_1|S_{1/2}\rangle_2) \tag{2}$$

$$\Phi_\pm = \frac{1}{\sqrt{2}}(|S_{1/2}\rangle_1|S_{1/2}\rangle_2 \pm |D_{5/2}\rangle_1|D_{5/2}\rangle_2) \tag{3}$$

set the basis states where the index indicates the ion number 1 or 2, respectively. These Bell states have been deterministically generated, starting from the ground state of vibration and electronic excitation. A sequence of a few steps of laser ion interaction with an overall duration less than 200 μs result in the production of any of these Bell states.

In the experiment [18], two $^{40}Ca^+$ ions are loaded into a linear Paul trap having vibrational frequencies of $\omega_{ax.} = (2\pi)1.2$ MHz in the axial and $\omega_{rad.} = (2\pi)$ 2.5 MHz in the transverse direction. After Doppler and sideband cooling the ions breathing mode of axial vibration is in the ground state $|n = 0\rangle$ with 99% occupation. Thereafter, both ions are initialized in the $|S_{1/2}\rangle$ ground state. For quantum state engineering, we employ laser pulses, tightly focused onto either one of the two ions. By exciting the transition $S_{1/2} \rightarrow D_{5/2}$ of a single ion, one generates a superposition of both states. If the laser excites the transition on resonance (carrier transition), the ion's vibrational state is not affected, whereas if the laser frequency is set to the transition's upper motional sideband (blue sideband), the electronic states become entangled with the motional states $|n = 0\rangle$ and $|n = 1\rangle$ of the breathing mode.

Starting in the state $|S_{1/2}\rangle_1|S_{1/2}\rangle_2|n = 0\rangle$, a $\pi/2$-pulse to ion 1 on the blue sideband results in $\frac{1}{\sqrt{2}}(|S_{1/2}\rangle_1|S_{1/2}\rangle_2|n = 0\rangle + |D_{5/2}\rangle_1|S_{1/2}\rangle_2|n = 1\rangle)$. Now, the second ion is addressed by a laser pulse driving a π-pulse on the carrier transition and leading to $\frac{1}{\sqrt{2}}(|S_{1/2}\rangle_1|D_{5/2}\rangle_2|n = 0\rangle + |D_{5/2}\rangle_1|D_{5/2}\rangle_2|n = 1\rangle)$. The third pulse, a π-pulse to ion 2 on the blue sideband, leads to $\frac{1}{\sqrt{2}}(|S_{1/2}\rangle_1|D_{5/2}\rangle_2|n = 0\rangle + |D_{5/2}\rangle_1|S_{1/2}\rangle_2|n = 0\rangle)$, because the transition from $|D_{5/2}\rangle_2|n = 0\rangle$ is impossible as the harmonic oscillator states end with $|n = 0\rangle$. The final state factorizes out the vibration and we end with the Bell state $\frac{1}{\sqrt{2}}(|S_{1/2}\rangle_1|D_{5/2}\rangle_2 + |D_{5/2}\rangle_1|S_{1/2}\rangle_2)$. Any of the Bell states is reached by minor modifications of the above scheme. A tomographic measurement reveals the full density matrix of the states [18], as shown in Fig. 2. Using an additional laser pulse, the $D_{5/2}$ part of the entangled two-ion wave function can be coherently transferred to the second Zeeman level in the ground state $S_{1/2}$, m=-1/2. Now, the Bell states are encoded in Zeeman $S_{1/2}$ ground state levels $\{+1/2, -1/2\}$ only [19], e.g. with the two-ion entangled state $\frac{1}{\sqrt{2}}(|+1/2\rangle_1|-1/2\rangle_2 + |-1/2\rangle_1|+1/2\rangle_2)$. States $\Psi_\pm$ of this type show 15 s lifetime, exceeding the time for generating these states by 5 orders of magnitude, an

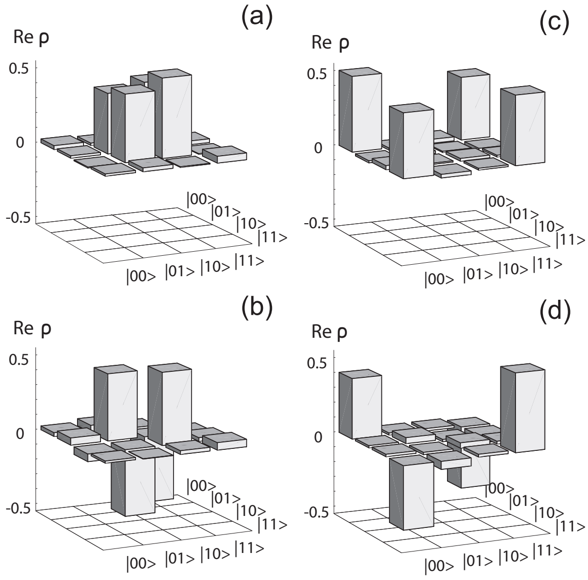

Fig. 2. – (a): Real part of the density matrix ρ_{Ψ_+} that approximates $\Psi_+ = (|10\rangle + |01\rangle)/\sqrt{2}$ with $S_{1/2} \equiv 1$ and $D_{5/2} \equiv 0$. The measured fidelity is $F_{\Psi_+} = \langle\Psi_+|\rho_{\Psi_+}|\Psi_+\rangle = 0.91$. (b): Real part of the density matrix ρ_{Ψ_-} that approximates $\Psi_- = (|10\rangle - |01\rangle)/\sqrt{2}$. The measured fidelity is $F_{\Psi_-} = 0.90$. (c),(d): Density matrix elements of ρ_{Φ_+} (c) and ρ_{Φ_-} (d). Here, $F_{\Phi_+} = 0.91$ and $F_{\Phi_-} = 0.88$.

impressive demonstration of decoherence-free basis sets [19]. Bell states within the $D_{5/2}$ Zeeman sublevels have been generated to design a two-ion entanglement optimal for the determination of the quadrupole shift.

3˙2. *Measurement of electric quadrupole shift in Ca$^+$ using entanglement.* – In ^{40}Ca$^+$, the magnetic sublevels of the $D_{5/2}$ state show a linear Zeeman shift. For a two-ion entangled state and if the two coherent parts of the Bell state experience an *identical* linear Zeeman effect, the phase evolution of the Bell state will be sensitive to much smaller corrections such as (i) the quadratic Zeeman effect (QZ) and (ii) the electric quadrupole (EQ) shift. The specific state used by Roos et al. [20] is

$$\Psi^{EQ} = \frac{1}{\sqrt{2}}(|-5/2\rangle_1|+3/2\rangle_2 + e^{i\Delta t}|-1/2\rangle_1|-1/2\rangle_2) \tag{4}$$

where the numbers indicate the Zeeman level in the $D_{5/2}$ manifold. The linear Zeeman shift of state in equ.4 vanishes. However, it experiences energy shifts due to the effect of QZ and EQ-interactions. This leads to a temporal phase evolution described by $e^{i\Delta t}$.

In the experiment, Ψ^{EQ} is generated by a sequence of laser pulses, see sect. **3**˙1. This quantum state evolves in phase under the action of the remaining interactions QZ and EQ. Please note that the corresponding energy shift of the order of 10^1 Hz is by 6 orders of magnitude smaller than the linear Zeeman shift which accounts for about 10 MHz in the 2.9 Gauss magnetic field in the experiment. Most important, when the magnetic field fluctuates slightly with time, the entangled state cancels out any of this variations, as the fluctuations affect both ions at a distance of only ~ 5 μm in an identical way. Similar to a differential probe for a sensitive measurement device, the use of entangled states allows for a huge *common mode rejection* of noise. To deduce the few Hz energy shift which stems from the interactions of interest, the phase evolution during an evolution time $0 \leq t \leq 300$ *ms* is observed by the parity signal of the Bell state, oscillating between $+1$

and -1. The observed period of $\Delta = (2\pi)$ 33.35(3) Hz allows extracting both, the electric quadrupole shift and an even smaller quadratic Zeeman shift, as the dependence of the frequency Δ is studied as (a) the axial trap frequency, thus the electric field gradient and (b) the direction of the magnetic field are systematically varied.

The remarkable high measurement accuracy with a sub-percent error results from the clever design of the Bell state. The method may be extended to design multi-ion entangled states such that further systematic shifts of the clock transition may be canceled equally well. Note, that the linear Zeeman effect is fully removed. Additionally, even the measured quadratic Zeeman shift of $\Delta = -(2\pi)$ 2.9 Hz in $^{40}Ca^+$ at B=2.9 Gauss is by two orders of magnitude reduced compared to that of e.g. the $^{199}Hg^+$ clock transition between $S_{1/2}$ m=0 and $D_{5/2}$ m'=0 states. The reason is that in case of Calcium, isotope 40, with nuclear spin I = 0 no hyperfine levels exist, such that only fine-structure levels can mix at high magnetic field strengths resulting in a quadratic Zeeman shift. Contrary, for the commonly used m=0 to m'=0 transitions of hyperfine clock states, orders of magnitude smaller magnetic interaction strength causes already level mixing in the hyperfine manifold and thus a quadratic dependence of Zeeman energy levels of the clock transition. Entangled states open therefore an entirely novel way for optical clock transitions including elements which have not been in consideration before.

3·3. *Heisenberg limited spectroscopy using entangled Be^+ ions.* – The weakest point about ion clocks might be their poor signal to noise ratio. Even though the experimental sequence takes only a few ms and is repeated quickly, the outcome of the result - ion was excited or ion was not excited - shows large *quantum projection noise*. Increasing the number of ions N will only improve gradually the signal to noise ratio as seen from the $1/\sqrt{N}$ dependence of the Allan frequency deviation of an atomic clock $\sigma(\tau)$ in equ. 1. Here, the advantage of probing a large ensemble of neutral atoms becomes obvious. However, it has been discussed that the entanglement of ions will allow to measure frequencies with improved signal to noise ratio of $1/N$ [21]. The effect of entangled states for spectroscopy might be explained with the multi-ion Dicke states. The Ramsey signal for a single ion depends on the accumulated phase shift between the phase of the laser field and the atomic superposition. With entangled states of the Greenberger Horne Zeilinger (GHZ) type $\frac{1}{\sqrt{N}}(|S\rangle_1|S\rangle_2...|S\rangle_{N-1}|S\rangle_N + |D\rangle_1|D\rangle_2...|D\rangle_{N-1}|D\rangle_N)$ the energy difference accounts for N times that for the single atom. Correspondingly, the accumulated phase shift increases N times faster and the oscillation period of the Ramsey signal decreases by the factor N. The narrower structure allows to pin down the frequency of the ion clock better by a factor of N.

The experimental realization uses three $^9Be^+$ ions [22]. State dependent forces are used to entangle the ions to a GHZ state. The second Ramsey pulse is a $\pi/2$-pulse to all ions. Then, the parity signal, the upper state population of all ions, is revealed (like step (ii) in the experimental sequence as described in sect. **2**). As expected from the theoretical considerations, a fringe period of $2\pi/3$ is observed. However, the contrast of the signal is reduced to 84% by the finite fidelity of the GHZ state, such that the experimental phase sensitivity increases by $0.84 \times \sqrt{3} = 1.45(2)$ instead of $\sqrt{3} = 1.73$. While the proof-of-principle experiment clearly demonstrates the effect, it remains to be applied in an ion-clock experiment. Larger numbers of ions in entangled states [24] have been generated with high fidelity but these states have not been applied for ion clocks.

Entanglement of GHZ states decays by decoherence N times faster than superpositions of a single ion. This has lead to a misleading argument that entanglement would not help improving ion clocks [23]. In the experimental reality, however, spontaneous decay of the ions from the excited upper clock level is just one, often an even minor source of decoherence such that a higher phase sensitivity of a N-ion GHZ state would help to increase the signal to noise ratio for shorter integration times. As long as the interrogation time is lower than the coherence time of the N-ion entangled state one can take advantage of the entanglement. As a consequence, the servo-loop for regulating the clock laser, see Fig. 1 attacks frequency deviations more quickly.

3˙4. *Readout of an Al^+ clock ion using quantum logic techniuqes.* – For any quantum gate operation between two ions [26, 27], the common vibration modes are used as quantum bus. Here it makes no difference of what species the trapped ion is. The common vibrational mode is used to optically cool and to read out the quantum state of a clock ion, whose cooling transition is not accessible by laser sources: While we do not know how to drive the dipole transition of $^{27}Al^+$ near 167 nm, this element possesses an ideal clock transition as it shares its advantages such like an insensitivity to magnetic fields and electric field gradients with the $^{115}In^+$ ion [25].

In the experiment, a single $^{27}Al^+$ ion and a single $^{9}Be^+$ ion are forming a crystal in a linear Paul trap [29]. In step (1) sideband ground state cooling is applied on the 313 nm Be^+ transition to reach $|n = 0\rangle$ of the common mode of vibration of both ions. (ii) The $^1S_0$ to $^3P_0$ clock transition of $^{27}Al^+$ is tested with a laser near 267 nm. The state ends, in general, in a superposition of clock states $^1S_0$ and $^3P_0$. (iii) A laser π-pulse on the red sideband of the Al^+-transition generates $|n = 1\rangle$, if and only if the excitation in step (ii) was successful. Thus, the superposition of clock states in the Al^+ ion is mapped on the vibrational mode $(\alpha|0\rangle + \beta|1\rangle)\sqrt{2}$. (iv) A red sideband π-pulse on the Be^+ transition is applied such that the Be^+ is excited only if the mode was excited to $|n = 1\rangle$ before. With this pulse the vibrational mode superposition is mapped on the Be^+ ion electronic states $\{|g\rangle, |e\rangle\}$. (v) Finally, the electronic state of the Be^+ is read by measuring its state dependent fluorescence. For this, light is scattered from the Be ion, which will emit fluorescence only if the ion is in the electronic state $|g\rangle$. This way, the clock transition frequency of a single $^{27}Al^+$ was determined with a relative error of 5×10^{-15}, corresponding to an uncertainty of 6 Hz [28].

In the Sect.**3** we have reviewed the significant progress in trapped ion optical clocks. Techniques developed in quantum information processing can be used to determine systematic frequency shifts such as the electric quadrupole and quadratic Zeeman shifts, to increase the signal to noise ratio of a Ramsey-type frequency measurement, and to read quantum states from clock ions which had been unaccessible with conventional methods. For a generation of entangled states of a larger number of ions and for improved operations of quantum processing, however, the standard design of the Paul traps needs to be modified.

4. – Modern segmented traps for scalable quantum information processing

In the last decade, we have seen a rapid evolution of ion traps: starting with three-dimensional cm-sized traps for hot clouds of ions, single ion traps with mm-sized ring-shaped or end-cap electrodes with sub-mm gaps have been investigated for quantum state engineering and spectroscopy. The conventional linear trap has been developed from the linear Paul mass filter which is commonly used. Only recently segmented linear micro traps, both in three dimensional and two dimensional form, have been developed.

Charged particles, such as atomic ions, can be confined by electromagnetic fields, either by using a combination of a static electric and magnetic field (Penning trap) or a time dependent inhomogeneous electric field (Paul trap) [30, 31]. In the latter case, an rf-electric field is generated by an appropriate electrode structure and creates a pseudo-potential confining a charged particle. The motion of a particle confined in such a field involves a fast component synchronous to the applied driving frequency (micro motion) and the slow (secular) motion in the dynamically created pseudo-potential. Fig. 3 shows as examples a selection of ion traps used at NPL, Teddington, England, at the Institute for Experimental Physics, University of Innsbruck, Austria and at the Institute for Quantum Information Processing, University of Ulm, Germany.

In order to confine the particle in a harmonic potential, we require an electric restoring force $\vec{F} = -q\vec{E}$, which increases linearly with the distance from the origin of the trap, e.g. $\vec{F} \propto -\vec{r}$. Such forces are described by a quadrupole potential $\Phi = \Phi_0(\alpha x^2+\beta y^2+\gamma z^2)/r_0^2$, where Φ_0 denotes a voltage applied to a quadrupole electrode configuration, r_0 is the characteristic trap size and the constants α, β, γ determine the shape of the potential, given by the solution of Laplace's equation $\Delta\Phi = 0$. For example, in the case of a *three-dimensional electric field* we find $\alpha = \beta = -2\gamma$. The potential is attractive in the x- and y-directions, but *repulsive* along the z-direction. A static electric field does not lead to three-dimensional binding. If, however, an alternating electric field is applied, the resulting potential is attractive in the x- and y-directions for the first half cycle of the field, and attractive in the z-direction for the second half. A well chosen amplitude and frequency Ω of this alternating rf-field then allows the trapping of charged particles, mass m and charge q, in all three dimensions. The three-dimensional Paul trap provides a confining force with respect to a single point in space, the node of the rf-field, and therefore is mostly used for single ion experiments or for the confinement of three-dimensional crystallized ion structures.

If we regard the electric rf-field in a *two-dimensional geometry* along x- and y- axis only, we find $\alpha = -\beta, \gamma = 0$. Here, the confining of a charged particle works only in the (radial) x, and y-direction. If an additional static dc-potential is applied in z-direction, the particle is trapped radially and axially, and we may talk about a linear ion trap. In order to realize a quantum register with trapped ions, a linear arrangement of the ions is advantageous. This geometry allows best individual observation, and individual coherent manipulation of an ion's quantum state. Specially adapted to the requirements of quantum information processing are segmented micro ion traps. Linear ion crystals may be shuttled, separated in single ions, or recombined by addressing the axial control electrodes with well suited voltages.

For the application of a single ion clock to the particular space mission SAGAS described later in this paper, a simple and reliable three-dimensional trap geometry similar to that shown in Fig. 3(a) is intended. It would operate as a frequency standard, with frequency data transmitted to Earth by laser link for comparison against an Earth-based ion clock. In future, and to take advantage of modern quantum technologies, here a micro ion trap might be better suited.

5. – Proposed space mission for tests of fundamental physics and exploration of the outer solar system

Space applications in fundamental physics, geodesy, time & frequency metrology, navigation are most promising using ion clocks. Onboard terrestrial or solar system satellites, their exceptional frequency stability and accuracy makes them a prime tool to test the fundamental laws of nature, and to study the Earth's and solar system gravitational potentials and their evolution. In the longer term, they are likely to provide the primary

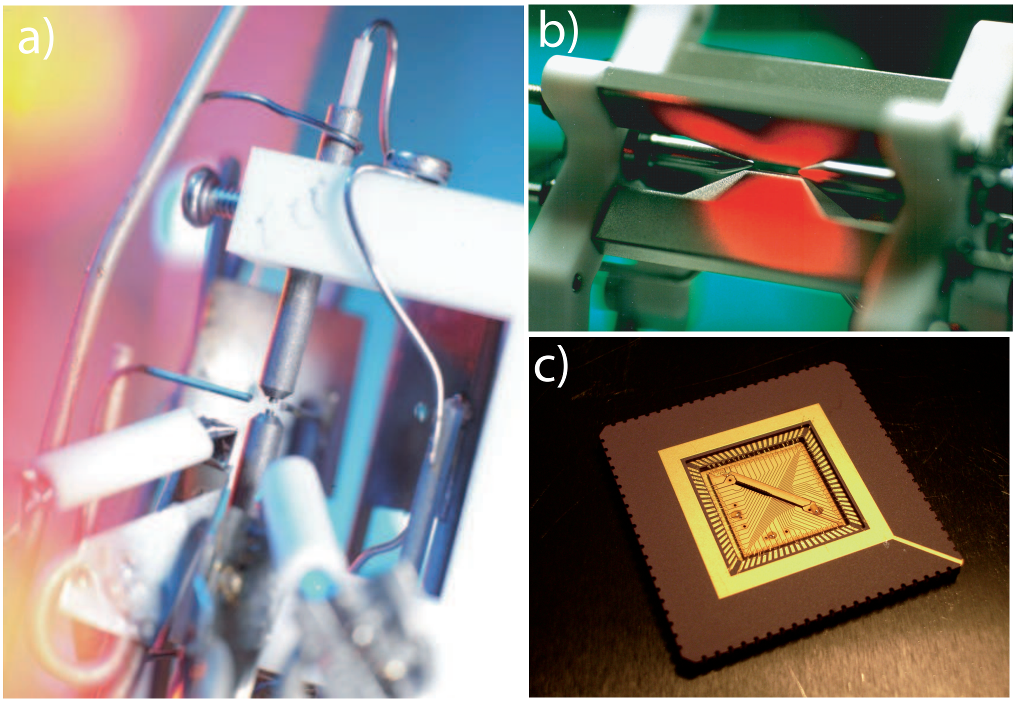

Fig. 3. – Various realizations of ion traps: a) Three dimensional NPL end-cap trap with 0.6 mm inner electrode separation [32] trap for single ion experiments. b) Innsbruck linear trap with four rf-electrodes in the shape of knife edges, axial electrodes in the shape of sharp tips. The free distance between two opposite knife edges is 1.5 mm, the distance between the axial confining tips is 5 mm [33, 34]. c) Ulm micro-ion trap with multiple segments for a full control of the axial trapping potential. The central slit with a width of 500 μm (left side) and 250 μm (right side) defines the region for ion trapping [35].

time reference for the Earth, as clocks on the ground will be subject to the less accurate knowledge of the geopotential on the surface [36]. For example, when comparing a clock on a low Earth orbiting satellite at 1000 km altitude to one on the ground they display a difference of 10^{-10} in relative frequency due to the relativistic gravitational frequency shift. Measuring that difference with 10^{-17} uncertainty would allow a test of the gravitational frequency shift to a few parts in 10^7 or equivalently, a determination of the potential difference between the clocks at the 10 cm level. The latter would contribute significantly to the knowledge of the geopotential and related applications in geophysics, representing the first realization of relativistic geodesy [37, 38] where the fundamental observable is directly the gravitational potential via the relativistic redshift. Similarly, comparing a clock on a solar system trajectory to one on the ground will allow tests of relativistic gravity and determination of the gravitational potential of celestial bodies with unprecedented accuracy.

Here we focus on a particular mission proposal, the SAGAS mission (Search for Anomalous Gravitation using Atomic Sensors). SAGAS will study all aspects of *large scale gravitational phenomena* in the solar system using quantum technology for its components which are a) the optical ion clock (S/C) optimized for long term performance with and uncertainty of $\leq 10^{-17}$ for 10-day integration times, b) an absolute accelerometer based on cold atom interferometry, c) two-way laser link for ranging, frequency comparison and communication with $\geq 10^{-17}$ stability for $\geq$10 day integration and d) ground ion clock [39]. The intended mission will contribute to answering some of the major questions of relevance to present day physics and space science:

- SAGAS will carry out a large number of tests of fundamental physics, and gravitation in particular, at scales only attainable in a deep space experiment. Given the scale and sensitivity of the SAGAS measurements, we will deeply probe the known laws of physics, with the potential for a major discovery in an area where many modern unification theories hint towards new physics. The unique combination of onboard instruments will allow 2 to 5 orders of magnitude improvement on many tests of special and general relativity, as well as a detailed exploration of a possible anomalous scale dependence of gravitation.

- It provides detailed information on the Kuiper belt mass distribution, the largely unexplored remnant of the circumsolar disk where the giant planets of the solar system formed, and determine the mass of Kuiper belt objects and possibly discover new ones. During the transits, the mass and mass distribution of the Jupiter system will be measured with unprecedented accuracy.

In the SAGAS proposal, the satellite would be launched using Ariane-5-ECA with an additional propulsion module that will be jettisoned after the first deep space manoeuvre. The satellite will be placed on a hyperbolic escape trajectory following gravity assists by Earth and Jupiter. Passing Jupiter 3.6 years after launch, it reaches the mission target heliocentric distance of 50 Astronomical Units (AU) in 19 years.

5˙1. *Clock segment based on a single trapped and laser cooled ion.* –
Selection criteria for the space ion clock
The single ion clock has been selected for the SAGAS mission as it has been demonstrating stabilities 7×10^{-17}@10^4 s and 3×10^{-17} accuracy with modest weight, volume and power consumption. Here, we have to choose among $^{199}Hg^+$,$^{171}Yb^+$,$^{88}Sr^+$,$^{40}Ca^+$,$^{115}In^+$, and $^{27}Al^+$ ions. In respect of quantum limited stabilities, the absence of a quadupole shift, a small black body shift, and small magnetic field sensitivity , J=0 $\rightarrow$ 0 clock transitions could be considered better choices for a high-specification clock system [15]. However, for continued long-term performance within the space mission environment, the ability to generate light for cooling and for clock transitions is the determinant. From this consideration we restrict ourselves to $^2S_{1/2} \rightarrow ^2 D_{3/2}$ transitions in either $^{171}Yb^+$,$^{88}Sr^+$, or $^{40}Ca^+$ ions. There is little difference in magnitude for the EQ (ea_0^2 from 1.8 to 2.6) or the blackbody shift (5.8 to 9.7×10^{-16}@ 300 K), thus, the maturity of laser technology needed to generate the necessary wavelengths determines the feasibility of the three choices.

Technological issues
The $^{171}Yb^+$ 436 nm clock transition [15] requires doubling stages for both clock and cooler. The fundamental wavelengths are not served well with available tapered amplifiers, with the cooling fundamental wavelength at 738 nm being particularly difficult. Additionally, there is the requirement for the clock laser wavelength to provide the link laser wavelength with $\sim$1 W of power, but no significant powerful source is currently

available. The $^{88}Sr^{+}$ 674 nm clock transition requires only one doubling stage from 844 nm to 422 nm. Sufficiently powerful extended cavity lasers with ∼150 mW output are now available such that relatively simple single pass doubling in periodically poled KTP can provide enough 422 nm power to provide all cooling beams. Narrow-linewidth probe lasers at the 674 nm clock transition are readily available with extended cavity diode lasers. Further, high power 674 nm tapered amplifier lasers are now available at the ∼0.5 W level, providing good opportunity for it use also as the link laser wavelength. Extended cavity diode lasers for probing the $^{40}Ca^{+}$ clock transition at 729 nm are available. Cooling of the ion at 397 nm can be achieved either by doubling 794 nm, tapered amplifiers exist so that single pass doubling should be possible. An alternative cooling arrangement is the use of a blue diode at 397 nm. High power tapered amplifiers also exist at the clock wavelength, offering opportunity for the link laser.

It can be seen that possibilities exists for all these three options. However, taking together the currently available power levels for both clock and cooler, the need for only one single pass doubling stage, clock laser linewidth and the clock accuracy already achieved, it is considered that the $^{88}Sr^{+}$ 674 nm clock represents the most feasible space ion clock option. The technology underpinning all three options has the capability to evolve in the near to medium term, and this should be a core component of technology refinement activity during early stages of a SAGAS mission preparation.

The $^{88}Sr^{+}$ ion clock system design and its sub-components

- Primary physics package, RF end-cap trap confining a single $^{88}Sr^{+}$ ion in ultra-high vacuum chamber pumped by a ion pump and non-evaporable getter pump. External magnetic field coils in 3 orthogonal axes allow the nulling of external fields, and setting of a fixed field. These coils are surrounded by mu-metal shielding to minimize external field changes.
- Laser for Doppler cooling to 1 mK dipole transition at 422 nm: A commercial extended cavity diode laser at 844 nm is frequency doubled in periodically poled KTP.
- Auxiliary lasers for repumping the ion from the $^{2}D_{3/2}$ metastable level during the cooling sequence, to ensure cooling continues, and for fast clear-out of the clock transition metastable $^{2}D_{5/2}$ upper level, once the clock transition has been driven. These are temperature- and current-stabilized DFB lasers.
- Clock laser probing the $^{2}S_{1/2} -^{2} D_{5/2}$ quadrupole clock transition at 674 nm. An extended cavity diode laser is frequency FM-stabilized to a very high finesse ultra-low-expansion cavity mounted on a temperature-stabilized, evacuated platform.
- High-NA lens imaging and photomultiplier detection system recording 422 nm fluorescence quantum jumps, providing the cold ion linewidth reference steering the clock laser.
- Fibre system to deliver the cooling, auxiliary and clock light from source to trap, making use of achromatic doublets where necessary at the fibre-free space interface for launching into the trap.
- Monitoring and control processor providing the primary cooling and clock laser pulse, magnetic field and detection sequencing to observe and lock to the ion clock

transition frequency. The processor also monitors frequency and amplitude data necessary to determine normal laser and ion operational conditions and initiate resetting and recovery algorithms where necessary, and laser unit failure.

- Heterodyne beat offset locking arrangement for slaving the 674 nm link laser to the 674 nm clock laser.

- Redundancy level of 2 units for both cooling, clock and high power link laser, plus a redundancy level of 3 units for the repumper and clear-out DFB lasers. All redundancy units for each wavelength to be fibre multiplexed as standard, allowing redundant unit activation on determination of prior unit failure mode.

$^{88}Sr^{+}$ ion clock performance and critical issues
An $^{88}Sr^{+}$ ion clock uncertainty of $\sim 10^{-17}$ is achievable within the spacecraft environment, provided external magnetic field and temperature variations are sufficiently low or adequately controlled. This requires μ-metal shielding of magnetic fields to allow the elimination of the EQ-shift. A temperature control of the trap apparatus and lasers with ± 0.5 K is necessary for control of the blackbody shift, and to maintain laser alignment. The sensitivity coefficient is $d(lnf)/dT = 3 \times 10^{-25}\ T^3/K^4$ so that for T=300 K, ΔT should be less than 2 K. The linear Zeeman effect accounts for ± 5.6 Hz/nT for the Δm=0 clock transition, but can be reduced to $\sim 10^{-17}$ using continuous Zeeman component pair averaging. Other effects like quadratic Zeeman shift, AC Stark shift, second order Doppler shift, and residual micro-motion add relative uncertainties of 10^{-18}.

Reloading of the trap will be necessary over a mission period of 15 years. A miniature Sr dispenser and a hot wire as an electron source are needed. Reloading of the trap will induce an interruption of clock operation for a few minutes. Charging problems of the trap and vacuum system will be avoided by illumination with ultraviolet LEDs. The discharge procedure will also be used periodically to eliminate charges from high energy radiation. For the clock we estimate an overall consumed electrical power of 80 W, a volume $\leq$180 l, and a total mass of 80 kg.

5·2. *Mission goals.* – Three fundamental measurements are provided: the accelerometer readout and the two frequency differences between ground clock and S/C measured between the incoming laser signal and the local optical clock. Auxiliary measurements are the timing of arriving signals on board and on the ground that are used for ranging and time tagging of data. The high precision science observables will be deduced from the raw frequency measurements (on board and on the ground) by combining them in two fundamental ways: Their difference yields sensitivity to the clock frequency difference with suppressed sensitivity to the motion of the S/C and ground clock and to atmospheric effects. Their sum yields sensitivity to the relative S/C - Earth velocity via the first order Doppler effect with suppressed sensitivity to the clock noise. The latter gives access to the gravitational trajectory of the satellite by correcting non-gravitational S/C motion using the onboard accelerometer readings and gravimetry and modern positioning techniques on the ground.

Test of the Gravitational Redshift and of Lorentz Invariance
In General Relativity (GR) the frequency difference of two ideal clocks is (to first order

in the weak field approximation)

$$\frac{d\tau_S}{dt} - \frac{d\tau_G}{dt} \simeq \frac{w_G - w_S}{c^2} + \frac{v_G^2 - v_S^2}{2c^2} + O(c^{-4}) \tag{5}$$

with w the Newtonian gravitational potential at the location of the clocks and v their coordinate velocity. In theories different from GR the relation (5) is modified, leading to different time and space dependence of the frequency difference. This can be tested by comparing two clocks at distant locations (different values of w and v) via exchange of an electromagnetic signal. At present the most sensitive such experiment [40] confirmed the GR prediction with a relative uncertainty of 7×10^{-5}. The SAGAS trajectory with a large potential difference and low uncertainty on the frequency difference observable (directly the difference in (5)) allows a relative uncertainty on the redshift determination given by the 10^{-17} clock bias divided by the maximum value of $(w_G - w_S)/c^2$. For a distance of 50 AU this corresponds to a test with a relative uncertainty of 1.0×10^{-9}, an improvement by almost 5 orders of magnitude.

The mission also allows testing the velocity term in (5), a test of Lorentz Invariance of Special Relativity, the so called Ives-Stilwell test. Towards the end of the nominal mission the corresponding term of $\sim 4 \times 10^{-9}$ can be determined by SAGAS with 3×10^{-9} relative uncertainty. We will improve the best present limit of 2.2×10^{-7} [41] by a factor ∼70. Considering a particular preferred frame, usually taken as the frame in which the 3 K cosmic background radiation (CBM) is isotropic, one can set an even more stringent limit. In that case a putative effect will be proportional to $(\overrightarrow{v}_S - \overrightarrow{v}_G).\overrightarrow{v}_{Sun}/c^2$ (cf. [41]), where v_{Sun} ∼350 km/s is relative to the CMB frame. Here, the mission will allow a measurement with about 5×10^{-11} relative uncertainty, corresponding to more than 3 orders of improvement on the present limit. Note that Ives-Stilwell experiments also provide the best present limit on a particularly elusive parameter $\tilde{\kappa}_{tr}$ of the Lorentz violating Standard Model Extension photon sector [42], hence the mission allows for a factor 70 to 10^3 improvement on that parameter.

Tests of Parameterized Post-Newtonian Gravity (PPN)

The PPN formalism describing a large class of metric theories of gravitation including GR in the weak field regime is well known (see eg. [43]) and has been extensively tested in solar system. The two most common parameters of the PPN framework are the Eddington parameters β and γ, both equal 1 in GR. Present limits on γ are obtained from measurements on light propagation such as light deflection and Shapiro delay. The tightest limit was deduced from Doppler ranging to the Cassini mission during solar occultation in June 2002 yielding $\gamma = 1 + (2.1 \pm 2.3) \times 10^{-5}$ [44]. SAGAS will carry out similar measurements during solar conjunctions, however with improved sensitivity and at optical rather than radio frequencies, which significantly minimizes errors due to the solar corona and the Earth's ionosphere. When the laser of the SAGAS link passes close to the sun the gravitational Shapiro delay leads to a maximum modification of the Doppler observable of about 8.5×10^{-10}. Optimal filtering of that signal in the estimated noise of the SAGAS observables leads to an uncertainty on the determination of γ of $\leq 1 \times 10^{-7}$, corresponding to more than two orders of magnitude improvement over present limits.

Exploring Large Scale Gravity

Experimental tests of gravity show a good agreement with GR at scales ranging from the millimeter in laboratory experiments to the size of planetary orbits. Meanwhile, most theoretical models aimed at inserting GR within the quantum framework predict observable modifications at smaller and/or larger scales. Anomalies observed in the rotation curves of galaxies or in the relation between redshifts and luminosities of supernovae are ascribed to "dark matter" and "dark energy" components, the nature of which remains unknown. These dark components, which constitute 96% of the content of the Universe, have not been detected by non-gravitational means to date. As the observed anomalies could also be consequences of modifications of GR at galactic or cosmological scales, it is extremely important to test the laws of gravity at the largest possible distances.

Tracking the orbit of the Pioneer 10/11 probes during their extended missions allowed for the largest scaled experimental test of gravity ever performed. The results failed to reproduce the expected variation of the gravity force with distance [45]. Precisely, the analysis of the radio-metric tracking data from the probes at distances between 20-70 AU from the Sun has shown the presence of an anomalous, nearly constant drift of the Doppler shift, interpreted as an unexpected acceleration of the order of 1×10^{-9} m/s^2, towards the Sun. The observation of this "Pioneer anomaly" (PA) has stimulated significant efforts to find explanations in terms of systematic effects on board the spacecraft or in its environment. The inability to explain the anomalous behavior of the Pioneer spacecraft with conventional physics [45] has contributed to the growing discussion about its origin, a discussion which is still ongoing [46]. It has also motivated an interest in flying new probes to the distances where the anomaly was first discovered, that is beyond the Saturn orbit, and studying gravity with modern techniques.

Over the past years a large number of theoretical frameworks that allow for a scale (distance) dependent modification of GR have been suggested, eg. generalized metric extensions of GR, Modified Newtonian Dynamics, Tensor-Vector-Scalar-theory, Metric-Skew-Tensor Gravity, $f(R)$ modified gravity theories, String theory and Cosmology motivated frameworks, Braneworld scenarios, and many others. It is far beyond the scope of this paper to study the effects of those frameworks on the SAGAS observables. A study under a number of conventional and "new physics" hypotheses can be found in [39]. It allows two main conclusions:

- With one year of integration all SAGAS observables allow a measurement of any effect of the size of the PA with a relative uncertainty of better than 1%. This will allow a "mapping" of any anomalous scale dependence over the $\sim$20 yr mission duration and corresponding distances.
- The complementary observables available on SAGAS (in particular S/C) allow a good discrimination between the different hypotheses thereby not only measuring a putative effect but also allowing an identification of its origin.

In summary, SAGAS offers the possibility to constrain a significant number of theoretical approaches to scale dependent modifications of GR. Given the complementary observables available on SAGAS the obtained measurements will provide a rich testing ground for such theories with the potential for major discoveries that may well lead to a revolution of relativity and physics as a whole.

Exploring Outer Solar System Masses

The Kuiper belt is a collection of masses, remnant of the circumsolar disk where giant planets of the solar system formed 4.6 billion years ago. Precise measurements of its mass distribution would significantly improve our understanding of planet formation

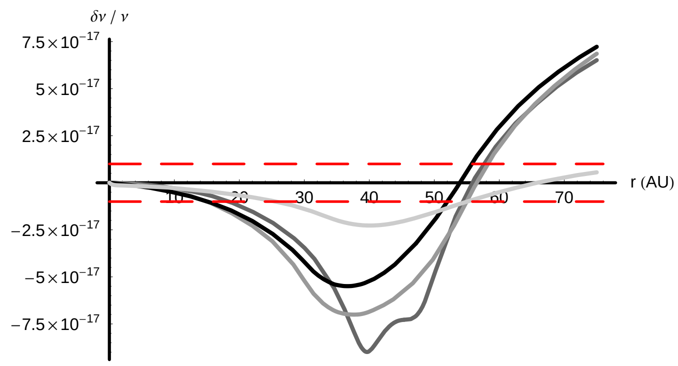

Fig. 4. – Relative frequency shift as a function of heliocentric distance from different Kuiper belt mass distributions, with a total mass of M_{KP}=0.3 M_E [39, 48]: Torus (black), Two rings (dark grey), Non-uniform disk (medium grey), Uniform disk (light grey). The red dashed lines indicate the uncertainty of the SAGAS clock.

not only in our but also in recently discovered planetary systems. The exceptional sensitivity and versatility of SAGAS for measuring gravity can be used to study the sources of gravitational fields in the outer solar system, and in particular the class of Trans Neptunian Objects (TNOs), of which those situated in the Kuiper belt have been the subject of intense interest and study over the last years [47]. Observation of Kuiper belt objects (KBOs) from the Earth is difficult due to their relatively small size and large distance, and estimates of their masses and distribution are accordingly inaccurate: Estimates from the discovered objects ($\sim$ 1000 KBOs) range from 0.01 to 0.1 Earth masses, whereas in-situ formation of the observed KBOs would require three orders of magnitude more solid material in a dynamically cold disk.

A dedicated probe like SAGAS will help discriminating different models of the spatial distribution of the Kuiper Belt and for determining its total mass. Figure 4 shows the relative frequency shift between the ground and space clock due to the Kuiper Belt gravitational potential $\delta\nu/\nu = w_{KB}(r)/c^2$, as a function of heliocentric distance of the S/C, and for several models of the spatial distribution of M_{KB} (see [39] for details).

Apart from the weaker delectability of the non-uniform disk mass distribution, the remaining models can be essentially detected from distances beyond 15 AU, and well discriminated at around 40 AU, well within the mission target distance. Furthermore, a complete "scan" over all distances available during the mission not only allows the determination of the shape of the curves shown on Fig. 4 and hence the mass distribution, but also the amplitude ie. the total mass M_{KB}. The accuracy of that will obviously depend on the distribution. For example, in the "two rings" distribution SAGAS will determine M_{KB} with an uncertainty of at least 10% ie. about 0.03 Earth masses. In a more detailed analysis one would fit all measurements during the mission to the candidate curve thereby likely decreasing the overall uncertainty by at most (depending on correlations of individual measurements) $\sqrt{N}$ where N is the number of measurements. Given that the clock noise integrates to 10^{-17} in about 10 days and for the 14 years travel from 15 AU to the end of the extended mission at 53 AU this leads to a $\sim$20$\times$ improvement.

The SAGAS frequency observable is well suited to study the large, diffuse, statistical mass distribution of KBOs essentially due to its sensitivity directly to the gravitational potential with $1/r$ dependence, rather than the acceleration with $1/r^2$ dependence. The large diffuse signal masks any signal from individual KBOs. When closely approaching one of the objects, the crossover between acceleration sensitivity (given by the 5×10^{-12} m/s^2 uncertainty on a_{NG}) and the frequency sensitivity (10^{-17} uncertainty

TABLE I. – *Science objectives of SAGAS*

Science Objectve	Expected Result	Comments
Test of Universal Redshift	1×10^{-9} of GR prediction	10^5 gain on present
Null Redshift test	1×10^{-9} of GR prediction	10^3 gain
Test of Lorentz Invariance (Ives-Stilwell test)	3×10^{-9} to 5×10^{-11},	10^2 to 10^4 gain, depending on trajectory
PPN test	$\delta(\gamma) \leq 2 \times 10^{-7}$	10^2 gain, may be improved by orbit modeling
Large Scale Gravity	- Fill data gap for scale dependent modif. of GR - Identify and measure PA to $< 1\%$ per year of data	Different observation types and large range of distances will allow detailed "map" of large scale gravity
Kuiper Belt (KB) Total Mass	$\delta M_{KB} \leq 0.03 M_{Earth}$	Dep. on mass distribution and correlation of clock meas.
KB Mass Distribution	Discriminate between common candidates	Will contribute significantly to solution of the "KB mass deficit" problem
Individual KBOs	$\delta M_{KBO}/M_{KBO} \leq 0.1$	dependent on distance of closest approach
Planetary Gravity	Jupiter gravity at $\leq 10^{-10}$	10^2 gain
Variation of Fund. Const.	$\frac{\delta\alpha}{\alpha} \leq (2 \times 10^{-4})\delta(\frac{GM}{rc^2})$	250-fold gain on present
Upper limit on Grav. Waves	$h \leq 10^{-18}$ (@ μHz-mHz)	Integration over one year

on $GM/(rc^2)$) for an individual object is situated at about 1.2 AU. Below that distance the acceleration measurement is more sensitive than the frequency one. This suggests a procedure to study individual objects using the SAGAS observables: use the S/C trajectory (corrected for a_{NG}) to study the gravity from a close object and subtract the diffuse background from all other KBOs using the frequency measurement. Investigating several known KBOs within the reach of SAGAS [39] shows that their masses can be determined at the % level when approaching any of them to 0.2 AU or less. Of course, this also opens the way towards the discovery of new such objects, too small to be visible from the Earth.

Similarly, during a planetary flyby the trajectory determination (corrected for a_{NG}) will allow the determination of the gravitational potential of the planetary system. The planned Jupiter flyby with a closest approach of ∼600000 km will improve present knowledge of Jovian gravity by more than two orders of magnitude [39].

Variation of Fundamental Constants

Spatial and/or temporal variations of fundamental constants constitute a violation of Local Position Invariance (LPI) and thus of GR [43]. Over the past few years there has been great interest in that possibility (see e.g. [49] for a review), spurred on the one hand by models for unification theories of the fundamental interactions where such variations appear quite naturally, and on the other hand by recent observational claims of a variation of different constants over cosmological timescales [50, 51]. Such variations can be searched for with atomic clocks, as the involved transition frequencies depend on combinations of fundamental constants and in particular, for the optical transition of the SAGAS clock, on the fine structure constant α. Such tests take two forms: Searches for a drift in time of fundamental constants, or for a variation of fundamental constants with ambient gravitational field. The latter tests for a non-universal coupling between ambient gravity and non-gravitational interactions (clearly excluded by GR) and is well measured by SAGAS because of the large change in gravitational potential during the mission.

For example, changing parameters of the standard model are usually associated with the effect of massless (strictly speaking, very light) scalar fields. One candidate, much discussed in the literature, is the dilaton, which appears in string models. Other scalars naturally appear in string-theory inspired cosmological models, in which our Universe is a "brane" floating in a space of larger dimensions. Such scalar fields would couple to ordinary matter and thus their non-zero value would introduce a variation of fundamental constants, in particular α of interest here. The origin of the non-zero value of such scalar fields could be cosmological [52, 53] leading to a constant drift in time of fundamental constants, and/or local, ie. taking ordinary matter as its source [54]. In the latter case one would observe a variation of fundamental constants with the change in local gravitational potential, which can be parameterized in the simple form [54] $\delta\alpha/\alpha = k_\alpha \delta\left(\frac{GM}{rc^2}\right)$. The best present limit on k_α is obtained in [54] from a comparison between a Hg^+ optical and Cs microwave clock, which have a sensitivity to the variation of α of -3.2 and +2.8 respectively. Monitoring their relative frequency as a function of the changing solar potential on the Earth's surface which is varying by $\delta(GM/(rc2)) \sim 3.3 \times 10^{-10}$ due to the Earth's eccentricity, a limit of $k_\alpha < 6 \times 10^{-7}$ was obtained. The difference in gravitational potential between the Earth and the SAGAS satellite at the end of nominal mission is 30 times larger than the variation attainable on Earth. The Sr^+ optical transition used in the SAGAS clock has a sensitivity to the variation of α of 0.43. When compared to a ground clock with 10^{-17} uncertainty this allows a limit of $k_\alpha < 2.4 \times 10^{-9}$, a factor 250 improvement over the best present limit.

Upper Limits on Low Frequency Gravitational Waves

Doppler ranging to deep space missions provides the best upper limits available at present on gravitational waves (GW) with frequencies of order c/L where L is the S/C to ground distance ie. in the $10^{-3..-5}$ Hz range [55, 57], and even down to $\leq 10^{-6}$ Hz albeit with lower sensitivity [56, 57]. The corresponding limits on GW are determined by the noise power spectral density (PSD) of the Doppler ranging to the spacecraft for stochastic GW backgrounds [56, 57], filtered by the bandwidth of the observations when looking for GW with known signatures eg. sinusoidal GW from binaries [55, 57]. In the former case best limits [57] are about $10^{-13}/\sqrt{Hz}$ in GW strain sensitivity at ~0.3 mHz, and in the latter case about $h \leq 2 \times 10^{-15}$ for the maximum amplitude of sinusoidal GW, again at 0.3 mHz. These limits increase rapidly at lower frequency [57].

A similar analysis can be carried out using SAGAS data, with the sensitivity limited by the noise on the Doppler observable [39]. This yields a strain sensitivity of $10^{-14}/\sqrt{Hz}$ for stochastic sources in the frequency range of 6×10^{-5} to 10^{-3} Hz with a f^{-1} increase at low frequency due to the accelerometer noise that could possibly be improved by modeling of non-gravitational accelerations. When searching for GW with particular signatures in the 6×10^{-5} to 10^{-3} Hz frequency region, optimal filtering using a corresponding

GW template will allow reaching strain sensitivities as low as $h \sim 10^{-18}$ with one year of data. This will improve on best present upper limits on GW in the $10^{-5..-3}$ Hz frequency range by about four orders of magnitude. It is not expected at present that GW with sufficiently large amplitudes are found, still the results might serve as upper bounds for astrophysical models of known GW sources, leaving open the door for potential surprises.

6. – Conclusion

Modern ion based clocks allow for testing important fundamental physics such as general and special relativity with unrivaled accuracy. Necessary technologies have been developed to an outstanding level of precision and reliability. The proposed mission SAGAS illustrates clearly the advantages of highly accurate clocks when flown on terrestrial or solar system satellites. Experiments like those performed by this mission are crucial for our knowledge of fundamental physics as well as measurements and exploration of gravity in the outer solar system. Table I summarizes all science objectives, showing the large quantitative improvements of the planetary mission SAGAS compared with previous knowledge. Other important applications of ion clocks in space to provide time & frequency standards for Earth applications such as navigation, or the application of quantum technologies e.g. for secure communication protocols have not been discussed here as they relate to satellites in terrestrial orbits.

In current and previous space missions to date, the focus has centered primarily on astronomy, Earth and planetary observation and geodesy, and biological, technological and even political aspects (cf the space race). Given the large costs involved in any space mission, the need for research in space is often questioned. In this paper, we have presented the possibilities for a space mission based on single ion clocks that looks to increase global understanding of fundamental physics. In such an endeavour, it is quite clear that the precision of state-of-the-art optical clocks together with their application within a space environment can offer significantly improved insights into fundamental physics over that which can be easily achieved on Earth, to the benefit of our understanding of the inter-relation between astronomy, planetary physics and cosmology.

* * *

FSK acknowledges support by the EU commission, the Baden-Württemberg Landesstiftung and the DFG. PG acknowledges the support of the EU Commission, ESA and the UK DIUS.

REFERENCES

[1] G. Santarelli et al., Phys. Rev. Lett. **82**, 4619 (1999).
[2] M. Takamato et al., Phys. Rev. Lett. **91**, 223001 (2003).
[3] M. Takamato et al., Nature **435**, 321 (2005).
[4] A. Brusch et al., Phys. Rev. Lett. **96**, 103003 (2006).
[5] V. Ovsiannikov et al.,Phys.Rev. **A 75**, 020501-R (2007)
[6] P. Gill et al., Meas. Sci. Technol. **14**, 1174 (2003).
[7] P. Gill et al., Phys. World **18** (5), 35 (2005).
[8] P. Gill, Metrologia **42** (3), 125 (2005).
[9] W. Itano, J. Res. Natl. Inst. Stand. Technol. **105**, 829 (2000).
[10] W. Itano etal., Phys. Rev. **A 73**, 022510 (2006).
[11] W. Oskay et al., Phys. Rev. Lett. **94**, 163001 (2005).

[12] W. Oskay et al., Phys. Rev. Lett. **97**, 020801 (2006).
[13] P. Dube et al., Phys. Rev. Lett. **95**, 033001 (2005).
[14] H. S. Margolis, et al., Science **306** 1355 (2004).
[15] T. Schneider, E. Peik, C. Tamm, Phys. Rev. Lett. **94** 230801 (2005).
[16] R. Rafac et al, Phys. Rev. Lett. **85**, 2462 (2000).
[17] S. Diddams et al., Science **293**, 825 (2001).
[18] C. Roos et al., Phys. Rev. Lett. **92**, 220402 (2002).
[19] H. Häffner et al., Appl. Phys. **B 81**, 151 (2005).
[20] C. Roos et al., Nature **443**, 316 (2006).
[21] D. Wineland et al., Phys. Rev. **A 50**, 67 (1994).
[22] D. Leibfried et al., Science **304**, 1476 (2004).
[23] S. Huelga et al., Phys. Rev. Lett. **79**, 3865 (1997).
[24] H. Häffner et al., Nature **438**, 643 (2005).
[25] C. Becker et al., Phys. Rev. **A 63**, 051802 R (2001).
[26] F. Schmidt-Kaler et al., Nature **422** 408 (2003).
[27] D. Leibfried et al., Nature **422** 420 (2003).
[28] T. Rosenband et al., Phys. Rev. Lett. **98**, 220801 (2007).
[29] P. Schmidt et al., Science 309, 749 (2005).
[30] W. Paul, Q. Osberghaus, and E. Fischer, Forschungsberichte des Wirtschafts—und Verkehrsministeriums Nordrhein-Westfalen **415** (1958).
[31] P. K. Ghosh, *Ion Traps*, The International Series of Monographs on Physics, 90. Oxford Science Publications (1995).
[32] G. P. Barwood, IEEE Transactions on Instrumentation and Measurement **56**, 226 (2007).
[33] S. Gulde, PhD Thesis, unpublished, Innsbruck (2003)
[34] F. Schmidt-Kaler et al., Appl. Phys. B: Lasers and Optics **77**, 789 (2003).
[35] F. Schmidt-Kaler and S. Schulz, Physik in unserer Zeit **4** (38) 162 (2007).
[36] P. Wolf and G. Petit, Astronomy and Astrophysics, **304**, 653, (1995).
[37] A. Bjerhammar, Bull. Geod., **59**, 207, (1985).
[38] M. Soffel, et al., Manuscripta Geodetica, **13**, 143, (1988).
[39] P. Wolf et al., arXiv:0711.0304 [gr-qc].
[40] R. F. C. Vessot et al., Phys. Rev. Lett. **45**, 2081, (1980).
[41] G. Saathoff et al., Phys. Rev. Lett. **91**, 190403, (2003).
[42] M. Hohensee et al., Phys. Rev. **D75**, 049902, (2007).
[43] C. M. Will, Living Rev. Relativity **9**, (2006).
[44] B. Bertotti, L. Iess, P. Tortora, Nature **425**, 374, (2003).
[45] J. D. Anderson et al., PRD **65**, 082004, (2002). O. Bertolami and J. Páramos, CQG **21**, 3309, (2004).
[46] C. Lämmerzahl, O. Preuss, H. Dittus, in *Lasers, Clocks, and Drag-Free: Exploration of Relativistic Gravity in Space*, H. Dittus, C. Lämmerzahl, S. G. Turyshev, (Eds.), p.75, Springer, (2007).
[47] A. Barucci, H. Boehnhardt, D. Cruikshank and A. Morbidelli, (Eds.), *The Kuiper Belt*, Univ. of Arizona Press, in press, (2007); in particular the chapter "The dynamical structure of the Kuiper Belt and its primordial origin" by A. Morbidelli.
[48] O. Bertolami and P. Vieira, CQG **23**, 4625, (2006); O. Bertolami and J. Pramos, gr-qc/0702149.
[49] J. P. Uzan, Rev. Mod. Phys. **75**, 403, (2003).
[50] M. T. Murphy, et al., Mon. Not. R. A. S., **345**, 609, (2003).
[51] E. Reinhold et al., Phys. Rev. Lett. **96**, 151101, (2006).
[52] T. Damour and K. Nordtvedt, Phys. Rev. Lett. **70**, 2217, (1993). Phys. Rev. **D48**, 3436, (1993).
[53] T. Damour and A. M. Polyakov, Nucl. Phys. **B423**, 532, (1994) [arXiv:hep-th/9401069].
[54] V. V. Flambaum and E.V. Shuryak, arXiv: physics/0701220, (2007).
[55] J. W. Armstrong et al., Astroph. J. **318**, 536, (1987).
[56] J. D. Anderson, B. Mashoon, Astroph. J. **290**, 445, (1985).
[57] J. W. Armstrong, et al., Astroph. J., **599**, 806, (2003).